Impacts of Radiation and Upper-Tropospheric Temperatures on Tropical Cyclone Structure and Intensity

BENJAMIN C. TRABING, MICHAEL M. BELL, AND BONNIE R. BROWN[a]

Colorado State University, Fort Collins, Colorado

(Manuscript received 12 June 2018, in final form 30 October 2018)

ABSTRACT

Potential intensity theory predicts that the upper-tropospheric temperature acts as an important constraint on tropical cyclone (TC) intensity. The physical mechanisms through which the upper troposphere impacts TC intensity and structure have not been fully explored, however, due in part to limited observations and the complex interactions between clouds, radiation, and TC dynamics. In this study, idealized Weather Research and Forecasting Model ensembles initialized with a combination of three different tropopause temperatures and with no radiation, longwave radiation only, and full diurnal radiation are used to examine the physical mechanisms in the TC–upper-tropospheric temperature relationship on weather time scales. Simulated TC intensity and structure are strongly sensitive to colder tropopause temperatures using only longwave radiation, but are less sensitive using full radiation and no radiation. Colder tropopause temperatures result in deeper convection and increased ice mass aloft in all cases, but are more intense only when radiation was included. Deeper convection leads to increased local longwave cooling rates but reduced top-of-the-atmosphere outgoing longwave radiation, such that the total radiative heat sink is reduced from a Carnot engine perspective in stronger storms. We hypothesize that a balanced response in the secondary circulation described by the Eliassen equation arises from upper-troposphere radiative cooling anomalies that lead to stronger tangential winds. The results of this study further suggest that radiation and cloud–radiative feedbacks have important impacts on weather time scales.

1. Introduction

Upper-tropospheric temperatures have been shown to be important for determining the maximum intensity that a tropical cyclone (TC) can reach, but the physical mechanisms through which the upper troposphere impacts TC intensity and structure have not been fully explored, due in part to limited observations and the complex interactions between clouds, radiation, and TC dynamics. A seminal theory on the potential intensity (PI) that a TC can attain was formulated by Emanuel (1986, 1988), who proposed that the PI was a function of sensible and latent heat fluxes from the underlying ocean and the temperature difference between the ocean and the outflow layer, which was initially considered to be the lower stratosphere. The derived PI equation assumes an axisymmetric and steady-state vortex and bases the formulation on the conceptual model of a TC as a Carnot heat engine. The primary constraint on PI is the balance between frictional dissipation and energy production in the inflowing boundary layer, with the upper-tropospheric "outflow temperature" formally providing an upper and outer thermodynamic boundary condition on a parcel erupting from the boundary layer in the eyewall. Conceptually, the outflow temperature determines the thermodynamic efficiency of the TC heat engine and can be regarded as the temperature of a radiative heat sink for the system.

The steady-state assumption in PI theory implies that a TC is in some statistical or radiative–convective equilibrium (RCE), and as such the impact of upper-tropospheric temperature modification on intensity has primarily been evaluated on long time scales >100 days in RCE (Emanuel et al. 2013). Ramsay (2013) analyzed the effects of colder tropopause temperatures on TC intensity using a nonhydrostatic, axisymmetric, cloud-resolving model in RCE over 120 days. Ramsay found that the maximum intensity of their 2D simulated TCs increased by $1\,\mathrm{m\,s^{-1}\,K^{-1}}$ cooling of the prescribed tropopause temperature and attributed this to the thermal efficiency change. Wang et al. (2014) performed a similar analysis in three dimensions using the Advanced Research version of the Weather Research and

[a] Current affiliation: TriVector Services Inc., Huntsville, Alabama.

Corresponding author: Benjamin Trabing, btrabing@colostate.edu

DOI: 10.1175/JAS-D-18-0165.1

Forecasting Model (WRF-ARW; Skamarock et al. 2008) to simulate how tropopause temperatures affect the intensity of TCs on both short and long time scales in RCE. The maximum intensity of their 3D TCs was found to increase by $\sim 0.5\,\mathrm{m\,s^{-1}\,K^{-1}}$ cooling on both short and long time scales but no structural difference was found between the TCs besides an upward shift in the outflow jet. A hypothesized difference between the rate of intensification per degree of tropopause temperature change for these two studies is due to the different experimental setups in two versus three dimensions and the temperature profiles used. Wang et al. (2014) showed that the inclusion of dissipative heating could also be a factor in changing sensitivity of the maximum tangential gradient winds to outflow temperature. Both of these studies validate a dependence of maximum intensity on upper-tropospheric temperatures in RCE but do not specifically diagnose the physical mechanisms that cause this dependence.

Both Ramsay (2013) and Wang et al. (2014) used simplified radiation schemes in the form of Newtonian cooling that did not explicitly include cloud–radiative feedbacks. The troposphere was cooled at a constant rate, while the upper troposphere and lower stratosphere were relaxed back toward a prescribed isothermal value on a time scale of 5 days. However, the physical mechanisms by which the upper-troposphere thermodynamic structure affects intensity in RCE with Newtonian cooling may be different than those on shorter time scales covering days to weeks with more complex radiative transfer (Hakim 2011). PI theory has been shown to be approximately valid for observed TCs when the local time tendency is small such that a quasi-steady-state framework can be applied (Bell and Montgomery 2008), although the complexities of the real atmosphere make diagnosing the impact of individual PI parameters very difficult. In this study, we employ a high-resolution, three-dimensional, full-physics model on a "weather" time scale of 8 days to diagnose the physical mechanisms behind why changing upper-tropospheric temperatures modify TC intensification, and to investigate the use of PI theory in understanding TC maximum intensity on weather time scales.

One potential mechanism by which a colder upper-tropospheric temperature could increase the TC intensity would be by allowing taller convection (Holland 1997). However, multiple studies have shown that convective available potential energy (CAPE) is generally unrelated to the steady-state intensity of idealized axisymmetric TCs (Camp and Montgomery 2001; Rotunno and Emanuel 1987; Emanuel 1989). We address this hypothesis through experiments using WRF ensembles with a combination of three different tropopause temperatures without radiation, such that the only change in the atmosphere is the initial thermal structure of the upper troposphere and lower stratosphere. As will be shown, these experiments do not show a consistent relationship between tropopause temperature and TC intensity, suggesting that radiation is a key element of this relationship.

Past studies have frequently neglected the effects of radiation on TCs because of the complexity it adds to the system (e.g., Nolan 2007), but inclusion of radiation has been shown to dramatically affect simulated TC structure and motion (Fovell et al. 2016). The role of radiation in affecting intensity is less clear and different mechanisms have been proposed. These mechanisms include differential heating between cloudy and cloud-free regions (Gray and Jacobson 1977; Craig 1996; Nicholls 2015), large-scale destabilization from longwave cooling (Dudhia 1989; Melhauser and Zhang 2014; Sui et al. 1998), changes in instability from radiative differences between cloud base and cloud top (Godbole 1973; Xu and Randall 1995), and longwave warming in clouds (Fovell et al. 2009; Bu et al. 2014). These mechanisms are not mutually exclusive, and multiple mechanisms may play roles in modifying TC intensity and structure at different stages of development and different times of the diurnal cycle (Dunion et al. 2014; Tang and Zhang 2016). In addition to the radiative impacts on convection, Navarro and Hakim (2016) and Navarro et al. (2017) have suggested that the effects of radiation on TC intensity can be discussed using a modified form of the Eliassen equation (Eliassen 1952) that describes the balanced response in the transverse secondary circulation to diabatic heating. Within the Eliassen framework, local sources of radiative heating and cooling lead to a modified secondary circulation that removes the diabatic anomalies and returns the system to gradient wind and hydrostatic balance. This framework is complementary to the Carnot engine perspective in PI theory, but with a distinct focus on local heating and cooling sources rather than on the system-scale heat source (sea surface temperature) and sink (outflow temperature).

We investigate these different conceptual frameworks and physical mechanisms in this study through experiments using idealized WRF ensembles that include longwave cooling and full diurnal radiation with shortwave heating. These experiments include cloud–radiative feedbacks that can alter both the convection and storm circulation, providing a means to test hypotheses on the role of both radiation and upper-tropospheric temperatures on TC intensity and structure on weather time scales. Our results suggest that colder upper-tropospheric temperatures produce stronger storms at a rate roughly consistent with PI theory, but that the physical mechanisms are complex and involve both convective and dynamical

interactions. As will be shown, a colder tropopause actually reduces the total radiative heat sink at the top of the atmosphere when including realistic longwave cooling due to the colder cloud-top emission temperature, but increases the local cloud-top cooling rate due to increased radiative flux divergence. The results suggest that the Eliassen framework is more appropriate when seeking to understand the impacts rather than a Carnot engine perspective. The actual maximum intensity of any particular ensemble member is sensitive to small moisture perturbations in the initial conditions, especially in the longwave-radiation-only experiments, suggesting that cloud–radiative feedbacks and stochastic interactions between convective elements also play an important role.

Section 2 will detail the setup of the idealized simulations and experiments. Section 3 will discuss how the upper-tropospheric temperatures and radiation impacted the intensity of the idealized simulations, followed by a description of the structural differences between the experiments in section 4. Section 5 will detail how the results of this study fit into the Carnot and Eliassen conceptual models, and section 6 will summarize the conclusions from this work.

2. Methods

In this study we conduct a series of idealized numerical simulations in an attempt to untangle the complicated interactions between clouds, radiation, and storm dynamics. The three-dimensional full-physics ARW (version 3.7.1; Skamarock et al. 2008) is employed using an idealized tropical cyclone setup that will be discussed in detail in the following paragraph. First, we construct environmental thermodynamic profiles based on observations as the initial conditions for our simulations. To make our idealized simulations semirealistic, three environmental input soundings are calculated from the National Centers for Environmental Prediction (NCEP) Climate Forecast System Reanalysis (CFSR; Saha et al. 2010). Since our goal is to understand the response of TCs to upper-tropospheric temperatures, we take advantage of the tropopause dependence on latitude, which descends and warms when moving poleward from the equator (Seidel et al. 2001). Monthly temperature products are averaged between 144°E and 180° during June, July, and August at three latitudinal bands of 10°, 20°, and 30°N. The calculation results in three mean thermodynamic profiles in the western North Pacific during the active part of the TC season with tropopause temperatures of 196.3, 199.6, and 202.9 K, respectively. These three thermodynamic profiles are then averaged below 200 hPa to isolate only the upper-tropospheric and stratospheric differences. Each profile is conditionally unstable and employs the same dewpoint temperature profile with moisture removed above 200 hPa. Figure 1 shows the initial sounding for each case with the cold-point tropopause (CPT) pressure level highlighted by the dashed black line denoting the top of the tropical tropopause layer (TTL) (Gettelman and Forster 2002).

The three different profiles are then used as initial conditions for idealized WRF simulations with two-way nested, doubly periodic domains with 18-, 6-, and 2-km resolutions in the horizontal. The outer domain extends 5400 km in the horizontal and the model top reaches 25 km with 30 vertical levels. A sensitivity test was conducted in which the vertical resolution was increased to 40 levels in select simulations, which changed the intensification rates of the TCs but not the conclusions of this study. Experiments are conducted over an ocean surface with no land and with sea surface temperatures (SSTs) fixed at 301 K. Models are initiated with no background wind and employ an *f*-plane approximation ($f = 5 \times 10^{-5}\,\mathrm{s}^{-1}$). Note that although the initial thermodynamic profiles are constructed from different latitudinal bands in order to vary the TTL, the Coriolis parameter is identical in all simulations. Simulations are initialized with a weak vortex using the method described in Rotunno and Emanuel (1987) and integrated for 8 days starting at 1200 local time (LT) 3 July. Physics options for the simulations include the Thompson aerosol-aware microphysics (Thompson and Eidhammer 2014), the Yonsei University planetary boundary layer scheme (Hong et al. 2006), the Rapid Radiative Transfer Model (RRTM) longwave radiation scheme (Mlawer et al. 1997), and the Dudhia shortwave radiation scheme (Dudhia 1989). The RRTM and Dudhia radiation packages are simplified but accurate parameterizations that account for multiple radiative bands and microphysics species interactions. The simulations use a solar constant of $1380\,\mathrm{W\,m^{-2}}$ and are fixed at 20°N. The coarse outer domain includes the new Tiedtke convective parameterization (Tiedtke 1989). The simulations employ the alternative surface-layer option for high-wind ocean surfaces to calculate the exchange coefficients for enthalpy and momentum; however, this parameter is not modified between simulations and does not include dissipative heating.

Approximately 3.3 K differentiates the CPT between each input sounding. This variation is small compared to the range of CPT values that Wang et al. (2014) implemented. In the RCE environment of their experiment, tropopause temperatures of 195 and 200 K showed no differences in peak tangential winds over the initial 8 days of their simulations with differences occurring in the time means over 100 days. On short time scales we expect the idealized TCs' intensities to be

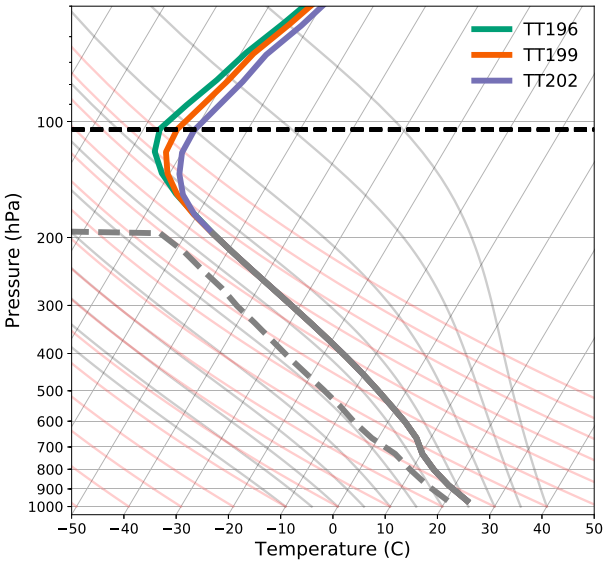

FIG. 1. Thermodynamic profile derived from NCEP CFSR data for each experiment on a skew T–log$p$ diagram. Below 200 hPa the profiles are averaged together, as indicated by the thick gray line. The gray dashed line indicates the dewpoint temperature profile. The horizontal black dashed line indicates the CPT pressure level.

sensitive to stochastic changes in convection (Van Sang et al. 2008). Therefore, due to model sensitivities and the relatively limited range of the derived thermodynamic profiles, an ensemble approach is taken to increase our confidence in the impacts of upper-tropospheric temperatures across multiple simulations. For each input sounding, 15 ensemble members are simulated using the method employed by Van Sang et al. (2008) in which random water vapor mixing ratio perturbations between -0.5 and $+0.5\,\mathrm{g\,kg^{-1}}$ are introduced to the lowest eta level. Introducing stochastic perturbations provides some spread in the TC intensity and structure after 48–72 h of model integration, allowing us to assess the sensitivity of upper-tropospheric temperatures and radiation to convection. The small water vapor perturbation in this idealized study is not meant to capture the full ensemble spread but rather the influences of stochastic convective elements. The delay in variability of ensemble members indicates a limited effect of the moisture perturbations on the initial spinup of the vortex, suggesting that intensity differences are due to stochastic interactions of convective elements later in the simulation. The simulations will herein be referred to by their CPT temperatures at model initialization (i.e., TT196, TT199, TT202) and the ensemble mean will be shown unless otherwise noted.

Three sets of experiments are conducted using the three derived thermodynamic profiles. One experiment includes both shortwave (solar) and longwave (infrared) radiation and will be referred to as Fullrad. The second experiment includes just longwave radiation and will be referred to as Nightonly. These results are then compared to simulations without radiation, which will be referred to as Norad. The full set of nine experiments is therefore a 3×3 parameter space consisting of three different TTLs and three different radiation physics that include cloud–radiative feedbacks not present in past studies that employed Newtonian cooling schemes in RCE, with 15 ensemble members for each experiment.

3. Intensity impacts

Figure 2 shows the evolution of the maximum axisymmetric tangential wind speeds for all experiments. The thick lines are the ensemble means and the hatched areas are the ensemble spread of plus and minus one standard deviation, indicating the variability due to the random water vapor mixing ratio perturbations in the initial conditions. The wind speed time series have been smoothed by a 1–2–1 filter for clarity. Figure 2 shows that each of the simulations undergoes a 12–24-h spinup time period before rapidly intensifying into an intense TC exceeding $80\,\mathrm{m\,s^{-1}}$. It is clear that to first order, the effects of radiation dominate over those of the modified TTL. The Nightonly simulations intensify the fastest, followed by the Fullrad and the Norad simulations, and the Nightonly simulations also attain the strongest maximum axisymmetric tangential wind speeds while the Fullrad and Norad simulations reach similar peak intensities. The effects of cooling on intensification rates in Nightonly can be attributed to differences in relative humidity and large-scale destabilization (Melhauser and Zhang 2014; Nicholls 2015). For the Fullrad simulations, the intensity peaks earlier than the other two radiation experiments and then decreases due to an eyewall replacement cycle, which occurred in all Fullrad simulations (not shown). It is reasonable to speculate that the Fullrad ensemble means would have achieved a peak intensity between the Nightonly and Norad means without the eyewall replacement, but the Norad means eventually peak slightly higher than do those of Fullrad. Radiative effects on secondary eyewall formation (SEF) are outside the scope of this study but have recently been discussed by Tang et al. (2017) and will be the subject of future work.

There are no discernible differences between $V_{\max}$ of TT196, TT199, and TT202 over the first 2 days of the Nightonly and Fullrad experiments, and over 3 days for the Norad simulations. The lack of differences over the early time periods indicates that upper-tropospheric temperature modifications have little effect on the TC vortex spinup. There also exists nearly no difference

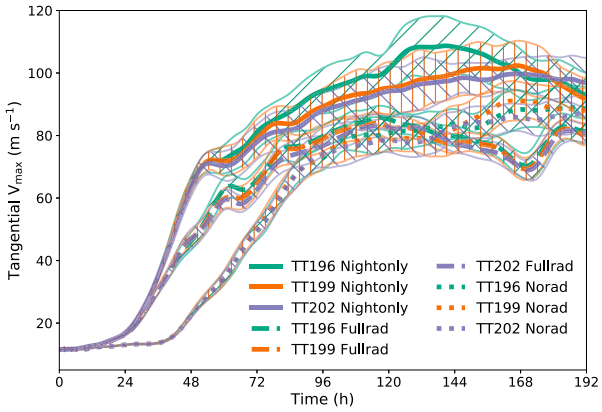

FIG. 2. Maximum axisymmetric tangential wind ensemble means for the Nightonly (solid), Fullrad (dashed), and Norad (dotted) simulations and plus and minus one standard deviation (hatched areas). Smoothed using 10 iterations of a 1–2–1 filter with weights of 0.25, 0.5, and 0.25, respectively.

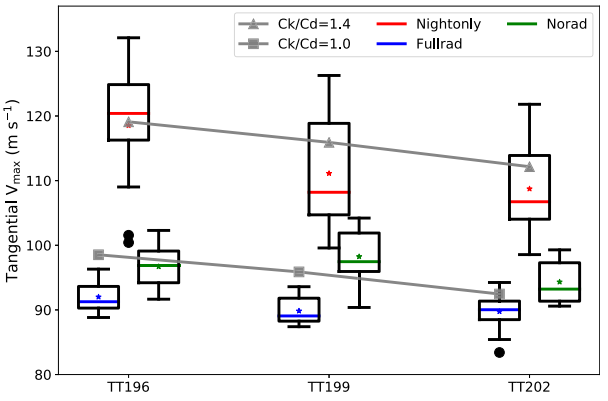

FIG. 3. Box-and-whisker plot of instantaneous axisymmetric tangential wind maximum for the Nightonly (red), Fullrad (blue), and Norad (green) ensembles. The colored lines indicate the median and the asterisks indicate the mean. The 25th–75th-percentile interval is indicated by the box with outliers in filled black circles where the distance between the box was greater than 1.5 times the width of the box. Gray lines are the theorized intensity based on PI (Bister and Emanuel 2002) using a ratio of exchange coefficients of 1.0 and 1.4.

in the standard deviations, indicating that stochastic changes in convection from the random moisture perturbations to the boundary layer also had negligible effects on TC genesis and early intensification. During the mature phase of the Nightonly and Fullrad simulations the maximum axisymmetric tangential winds increase with decreasing upper-tropospheric temperatures, but in the Norad simulations there is no clear relationship and TT199 is the most intense. The variability of the experiments increases at later times with the Nightonly simulations showing the largest spread and the Fullrad simulations showing the smallest variability. The ensemble variance and difference between the Fullrad means is small; however, a two-sided t test reveals statistically significant differences at the 95% confidence interval between TT196 and TT202 over most times between 48 and 120 h. In the Nightonly simulations, there are larger differences in means but also a larger variance in ensemble means between TT196 and TT202. Simulations TT196 and TT202 are statistically different; however, the null cannot be rejected when comparing TT199 and TT202.

We can directly compare the theoretical PI and the maximum intensity of the idealized simulations by analyzing Fig. 3. The box-and-whisker plot shows the ranges of the maximum, instantaneous, axisymmetric tangential winds of the simulations, with the 25th and 75th percentiles of the distribution indicated by each box and the median of each experiment denoted by the colored lines. The maximum 10-m winds were also considered and show the same relationship scaled by roughly a factor of 0.8. The expected theoretical PI for the given environment is calculated using the approach of Bister and Emanuel (2002) from the profiles shown in Fig. 1. The expected theoretical PI includes dissipative heating, although it is not included in the simulations, and is denoted by the gray symbols. The inclusion of dissipative heating increases the theoretical maximum intensity to better compare the winds, which may be supergradient. The gray squares assume that the ratio of exchange coefficients (C_k/C_D) is unity and the gray triangles assume $C_k/C_D = 1.4$. We note that C_k/C_D at high wind speeds is still highly uncertain and may be lower than the values shown (Bell et al. 2012), such that the two gray lines are used to illustrate the dependence of PI on changing outflow temperature and not as an absolute estimate of the PI intensity. The theoretical PI lines show comparable, but slightly different, slopes for increasing maximum axisymmetric tangential winds with upper-tropospheric cooling for the Nightonly and Fullrad simulations, while the Norad intensities are not consistent with the theory on weather time scales. If we consider the ensemble means for the experiments with radiation, we get relationships of $\sim -0.3\,\mathrm{m\,s^{-1}\,K^{-1}}$ for Fullrad and $\sim -1.5\,\mathrm{m\,s^{-1}\,K^{-1}}$ for Nightonly experiments. The theoretical relationship is between 0.5 and $0.9\,\mathrm{m\,s^{-1}\,K^{-1}}$ for $C_k/C_D = 0.5$–1.5 at a constant SST of 301 K, which is similar to the theoretical values found by Wang et al. (2014). The TTL cooling to the PI relationship from our Nightonly simulations is larger than expected from the range given by PI theory and the $\sim$0.4–$0.5\,\mathrm{m\,s^{-1}\,K^{-1}}$ of cooling for the PI increase found by Wang et al. (2014). The Fullrad simulations show comparable magnitudes of TTL cooling to the PI increase found in Wang et al. (2014). Differences in the

rates between our experiments and over the first 8 days of the simulations by Wang et al. (2014) are likely due to the treatment of radiation, cloud–radiative feedbacks, and differences in the temperature profiles.

The Nightonly simulations are the most sensitive to the ensemble perturbations and have a very large intensity spread compared to the other two radiation experiments. While the intensity is more likely to be higher with a colder TTL in the Nightonly simulations, the ensemble variability suggests the actual intensity of any one member depends strongly on the stochastic interactions of convective elements. We hypothesize that the higher variability is due to more favorable conditions for deep convection from the longwave cooling, and also to potential vortex instability at these extreme intensities. Comparisons between the strongest and weakest ensemble members indicate that stronger members have increased snow aloft at higher altitudes (not shown), suggesting that some members were randomly able to better organize the convection to reach a higher intensity than others. Shortwave heating in the Fullrad simulations appears to have helped counteract this effect since the Fullrad ensembles are weaker and exhibit very little variability due to the moisture perturbations. These results have interesting implications for the impact of radiation on the intrinsic predictability of intensity, but this is outside the scope of the current investigation.

Radiation plays an important role in maintaining the temperature balance of the atmosphere (Emanuel 1989) and is critical in longer-time-scale simulations such as those conducted by Ramsay (2013) and Wang et al. (2014). By neglecting radiation in the Norad experiments, we potentially introduce unrealistic structures in the thermodynamics that are not found in nature, but we are able to remove many of the complexities associated with cloud–radiative feedbacks. We assume here that differences between our Norad ensembles can be attributed to the direct impact of upper-tropospheric temperature differences on the height of the TC and its convection. Due to the variability of the intensities and the small difference between the Norad ensemble means, the null hypothesis that the ensemble means are the same cannot be rejected at the 95% confidence interval using a two-sided t test. Since the Norad mean intensities are not statistically different and do not show an increase in maximum wind speeds with colder upper-tropospheric temperatures, it is reasonable to conclude that radiative effects are a critical aspect of the relationship between upper-tropospheric temperatures and intensity. We can therefore tentatively reject the hypothesis that the height of the convection *alone* is responsible for the relationship. Further analysis of the differences in the structure of the simulations will further confirm this conclusion.

4. Structure impacts

a. Structure of no-radiation experiments

To compare the TC structures in the different experiments we examine 24-h ensemble means of the azimuthally averaged structure during intensification and at peak intensity to isolate slowly evolving, coherent structures and remove transient features on the convective or diurnal time scales. Figure 4 shows 24-h axisymmetric averages of the Norad ensemble simulated 10-cm radar reflectivity, potential temperature θ, and secondary circulation for the intensification phase between 48 and 72 h and when the TCs reached peak intensity between 144 and 168 h. The total ensemble mean from all Norad simulations (45 members) is shown in Figs. 4b and 4e, with the mean anomalies for the 15 ensemble members in the TT196 (Figs. 4a,d) and TT202 (Figs. 4c,f) experiments. The 15-member ensemble mean of the TT199 experiments is very similar to the total 45-member ensemble mean and is not shown.

During the intensifying phase (Fig. 4, top) the secondary circulation wind vectors indicate vertical motion in an outward tilted eyewall with radial inflow in the boundary layer and radial outflow around 13 km. The radius of maximum winds (RMW) is near 30 km at the surface and tilts outward with height, and the isentropes are beginning to descend in the eyewall and eye as the TC warm core grows in strength. Differences in structure caused by modifying the upper-tropospheric temperature in TT196 and TT202 are illustrated by the anomalies in Figs. 4a and 4c. During the intensification phase the largest differences are seen in upper-level θ anomalies, which reflects modifications in the initial temperature profile. Higher reflectivity is also found at the upper edge of the clouds above the eyewall in TT196 and reduced reflectivity in TT202. The reflectivity difference corresponds to a change in the storm-top height where TT196 is taller and TT202 is shallower. Additionally, there are anomalies in the secondary circulation near the outflow region that develop as the TCs intensify. In TT196 the outflow is strengthened near the reflectivity anomaly and is weakened below it, while in TT202 the opposite occurs. The confined location of the anomalies to upper levels corresponds to an increase in height of the outflow level consistent with the modeling study of Wang et al. (2014).

At peak intensity (Fig. 4d–f) the Norad ensemble mean has stronger vertical motion in the eyewall, a stronger reflectivity core, and a full-tropospheric warm

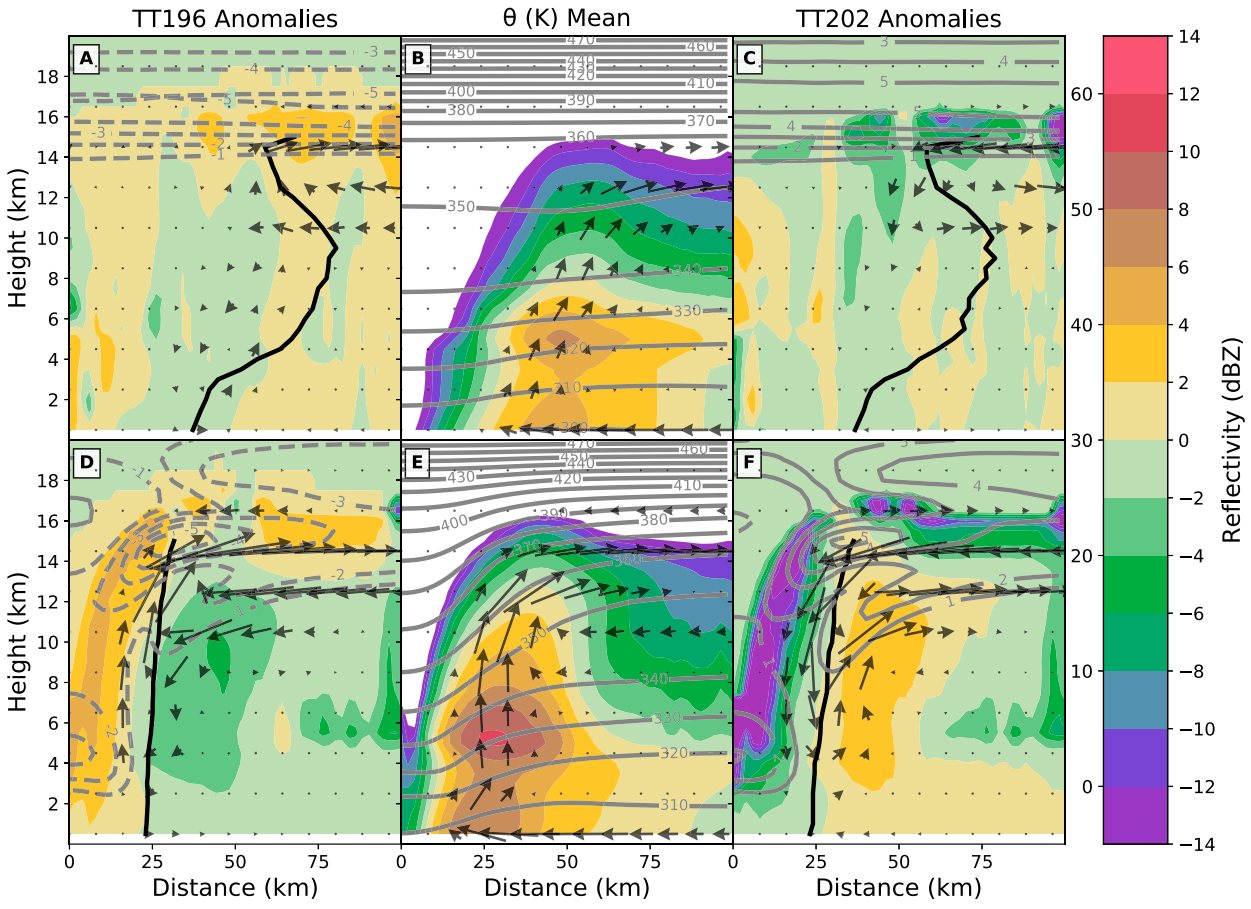

FIG. 4. Axisymmetric mean potential temperature θ (contoured) and reflectivity (shaded) for Norad simulations during hours (a)–(c) 48–72 and (d)–(f) 144–168. Shown are (b),(e) the ensemble means with θ contours every 10 K and reflectivity shaded every 5 dBZ with reflectivity below −5 dBZ whited out, (a),(d) the anomalies of TT196 from the ensemble mean, and (c),(f) the anomalies of TT202. The θ anomaly contour interval is 1 K and the zero line has been removed for clarity. Negative θ anomalies are dashed. Black line indicates RMW up to 15 km. Secondary circulation is denoted by wind vectors with magnitudes less than 1 m s^{-1} removed. The wind vectors have been increased by a factor of 3 in the vertical only.

core. The RMW has contracted to <25 km and is nearly vertical, highlighting the compactness of the simulated TCs without radiation (Fovell et al. 2016). A layer of radial inflow has developed both below and above the outflow layer at 14 km. The reflectivity and secondary circulation anomalies seen at peak intensity in Fig. 4 are similar to those found during the intensifying period, but with an added change in the radial direction. The TT196 mean eyewall is both higher and radially inward of the TT202 mean eyewall, as evidenced by the dipole signature in the reflectivity and anomalous circulation in the outflow and eyewall updraft. The radial and vertical displacement of the eyewall does not explain the anomalous potential temperatures in the eye. The θ anomalies show that the mean warm core of TT196 is weaker compared to that of TT202 and that the initial upper-tropospheric temperature differences have persisted. Without radiation, θ anomalies prescribed at the beginning of the simulation are advected downward by the upper-level secondary circulation, such that the colder TTL stays colder aloft and the warmer TTL stays warmer.

The Norad experiment analysis indicates that without radiation the height and radial extent of the TC are modified by upper-tropospheric temperatures. The change in height response to changes in upper-tropospheric temperatures is consistent with parcel theory and was noted by Wang et al. (2014); however, the θ anomalies introduced in the TTL due to the change in tropopause height are then advected downward by the secondary circulation and modify the warm core. It is generally recognized that the magnitude of the warm core increases with the intensity of a TC due to thermal wind balance (Ohno et al. 2016); however, even though TT196 and TT202 have similar intensities, θ anomalies in the warm core are approximately 5 K different. One hypothesis for explaining this difference

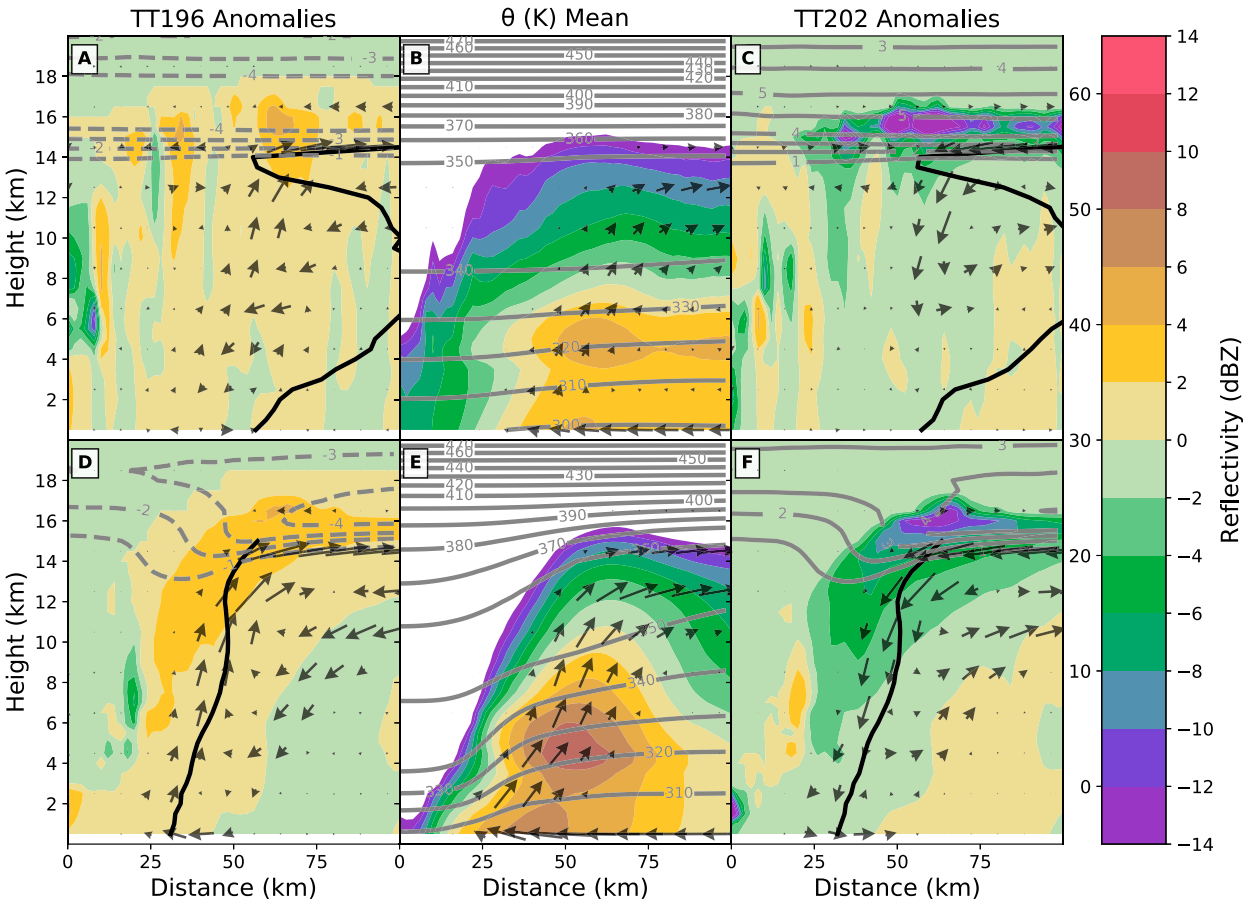

FIG. 5. As in Fig. 4, but (a)–(c) during the intensifying phase (24–48 h) and (d)–(f) at peak intensity (96–120 h) for the Fullrad simulations.

is that the hydrostatic surface pressure fall is dependent on both the magnitude and height of the warm core (Hirschberg and Fritsch 1993), such that these two effects offset each other to some extent in these simulations. It is unclear exactly how the warm-core anomalies contribute to the intensities in the Norad experiment, but the secondary circulation anomalies do not increase at low levels. Without low-level support to increase the surface tangential winds through the convergence of angular momentum surfaces, increasing the height of the storm is not sufficient to increase the intensity of the storm by itself.

b. *Radiative impacts*

Figure 5 shows 24-h axisymmetric averages of the Fullrad experiments for the intensification period (24–48 h) and at peak intensity (96–120 h) similar to Fig. 4. The effects of both shortwave and longwave radiation cause broader storms compared to the Norad simulations, with increased eyewall tilt consistent with recent modeling studies (Nicholls 2015; Fovell et al. 2016). The initial difference in upper-tropospheric θ is evident and is similar in magnitude between TT196 and TT202. The reflectivity anomalies present above the eyewall primarily indicate the heights of the TCs differ due to differences in upper-tropospheric temperatures where TCs with colder upper-tropospheric temperatures yield increased ice at an elevated altitude similar to the Norad simulations. Anomalies in the secondary circulation initially occur at upper levels in the Fullrad simulations with a similar pattern as the Norad simulations; however, the anomalies extended farther downward than the simulations without radiation.

At peak intensity the broader Fullrad simulations have a more tilted eyewall compared to that of Norad, and the outflow occurs throughout a deeper layer but does not have any inflow below or above the outflow jet. The warm core in the Fullrad simulations is strongest near the base of the eye and extends over a larger region compared to that of Norad. The Fullrad TT196 anomalies show the same toroidal motion in the outflow layer with enhanced outflow aloft and anomalous inflow just below that descends along the outer edge of the eyewall. A key difference between Norad and Fullrad is that the secondary circulation anomalies in the Fullrad

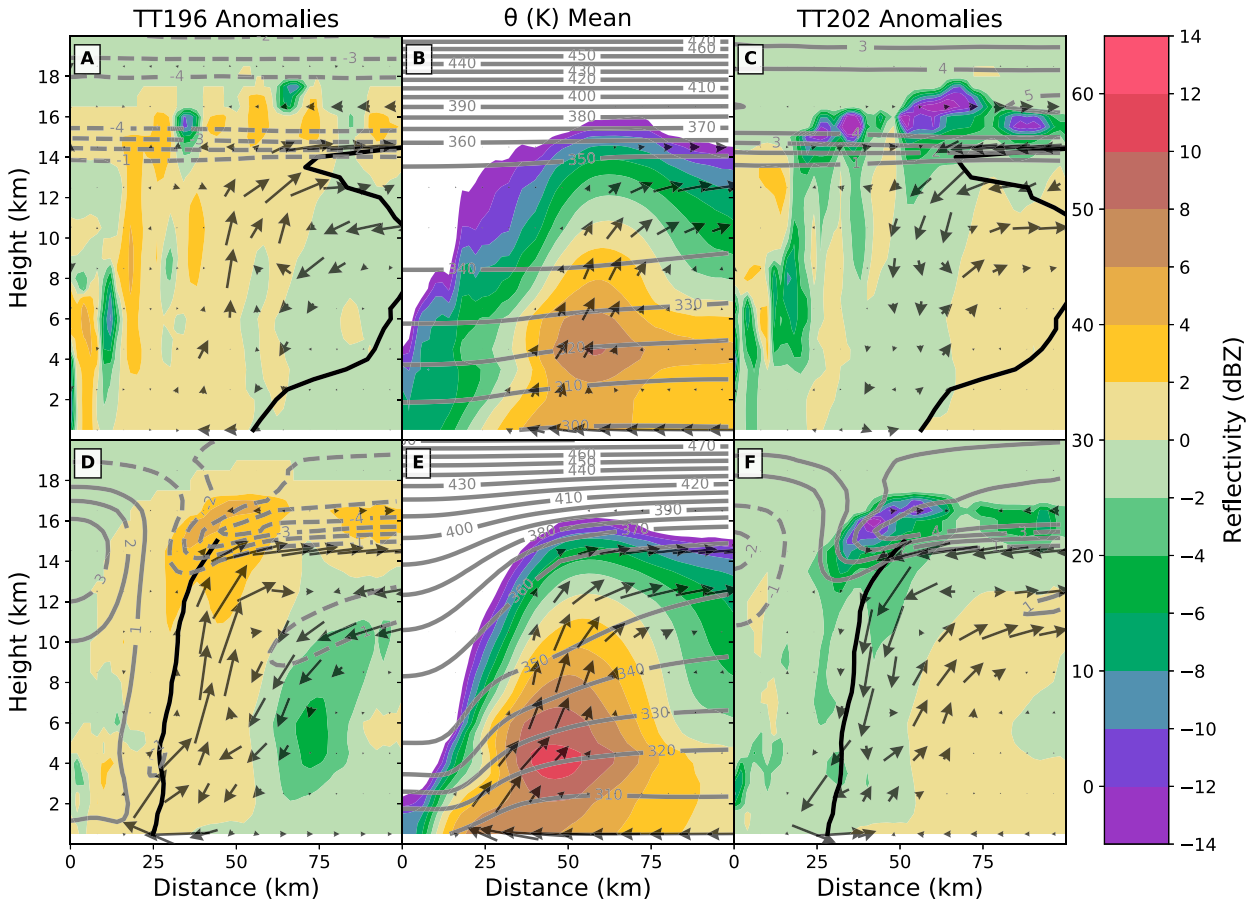

FIG. 6. As in Fig. 4, but (a)–(c) during the intensifying phase (24–48 h) and (d)–(f) at peak intensity (120–144 h) for the Nightonly simulations.

experiment extend throughout the vertical extent of the eyewall while the Norad anomalies do not reach below 4 km. The overall θ anomalies are reduced compared to the Norad simulations due to the effects of radiation. The reduction in overall intensity of the warm core and SEF may also contribute to the lack of anomalous warming in the Fullrad eye that could have possibly developed at a later time.

Figure 6 shows the same axisymmetric mean profiles as Fig. 4 for the Nightonly simulations. The Nightonly ensemble mean and anomalies are similar to the Fullrad simulations during the intensifying 24-h period shown, with differences growing over time as the simulations intensify at different rates. At peak intensity the θ anomalies in the eye of the Nightonly simulations are distinctly different from those of both the Fullrad and Norad simulations. In the TT196 simulations the warm-core potential temperatures become enhanced while the warm core in TT202 is reduced, particularly at upper levels. The secondary circulation also evolves in a manner similar to Fullrad but with different magnitudes of both the ensemble mean and anomalies. Anomalies in the secondary circulation are found at upper levels that cause stronger outflow in TT196 and weaker outflow in TT202 similar to the Fullrad experiment, but there is an even stronger anomaly near the surface. We attribute the differences in θ and secondary circulation anomalies between the Norad, Fullrad, and Nightonly simulations to the differing feedbacks between the TTL structure and the radiative heating and cooling.

c. *Mass transport by secondary circulation*

The structure of the simulations shows anomalous circulation patterns that we will now examine in more quantitative detail by examining the vertical and radial mass fluxes. Figure 7 shows the mean positive vertical mass flux over the 48 h prior to peak intensity of each experiment and the anomalies. The vertical mass fluxes in the Nightonly simulations are stronger than those of Fullrad, which are in turn stronger than those of Norad. The lower vertical mass flux in the Norad simulations is largely a product of the smaller storm size. Stronger

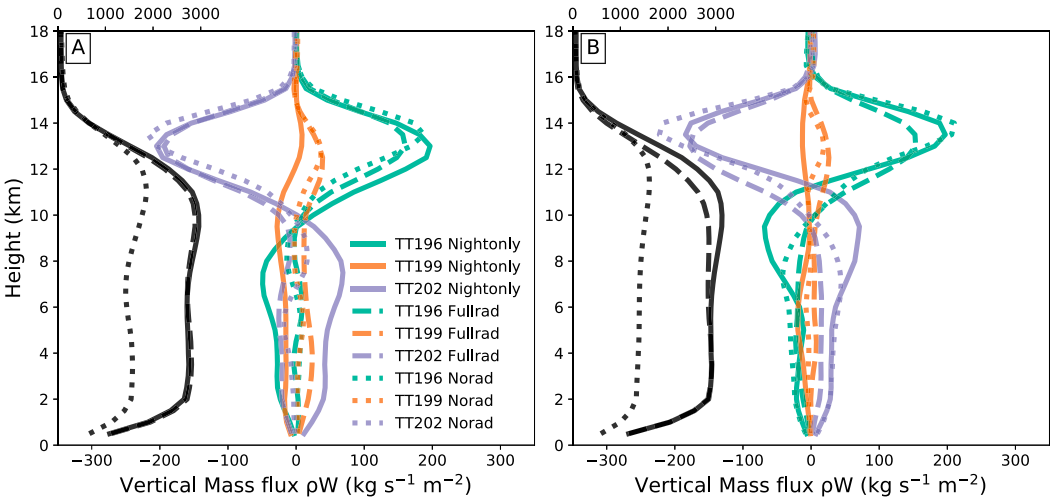

FIG. 7. Total upward vertical mass flux (kg s^{-1} m^{-2}) means (black) and anomalies between radii of 0 and 100 km for (a) 48–24 h prior to peak intensity and (b) 24 h prior to peak intensity. Profiles are taken from ensemble means of the Nightonly (solid), Fullrad (dashed), and Norad (dotted) simulations. The ensemble means (anomalies) are plotted according to the top (bottom) abscissa.

low-level mass fluxes in the Nightonly simulations support the results of Navarro and Hakim (2016) in which increased low-level diabatic heating in the eyewall was found to occur indirectly from longwave radiation. Anomalies in the vertical mass flux show very similar patterns between each of the ensembles, indicating that a key effect of the upper-tropospheric temperature structure is to modify the upper-level mass flux. Colder upper-tropospheric temperatures yield more upper-level mass flux with the opposite occurring due to warmer temperatures. The anomaly is consistently weaker for the Fullrad simulation compared to the Nightonly simulation and maximizes at a slightly lower altitude, which can be attributed to the competing effects of destabilization by longwave cooling and stabilization by shortwave heating.

Figure 8 shows the mean and anomalous radial mass flux as a function of time for each experiment. First focusing on the means (middle row), Fig. 8 shows that the radial inward mass flux is much stronger in the Nightonly simulations compared to both the Fullrad and Norad experiments and persists much longer. The Fullrad simulations have the weakest outward mass flux, which weakens due to the SEF. The Nightonly and Norad experiments have similar outward mass flux magnitudes with the Norad outflow becoming stronger on average at later time periods. The anomalies in radial mass flux are considerably different for the different radiation schemes. In the Nightonly experiment, TT196 has an overall stronger outward mass flux than TT202, while in Fullrad there are only weak differences between TT196 and TT202. The Norad simulations have a dipole in which TT196 has stronger outward mass flux but compensates with anomalous inward mass flux below it. The dipole reverses in TT202, which provides further evidence that in the Norad simulations there is a shift in height of the outward mass flux while in Nightonly and Fullrad there is both a change in the strength of the outward mass flux and a shift in height.

Figure 9 shows the integrated radial mass flux for two different radii–height cross sections extending from 0- to 100-km radius. The dashed line is the radial mass flux integrated from 0- to 3-km height and represents the strength of the inflow. The solid line is integrated from 8- to 16-km altitude and represents the strength of the radial outward mass transport or outflow. Comparing the area of the outward and inward mass flux lines indicates the strength of the secondary circulation and the total mass transport by the TC. The ensemble means show that Nightonly has both stronger radial mass flux into and out of the eyewall. The Fullrad simulations have stronger radial mass flux compared to the Norad simulations before the SEF.

Examining the anomalies, it is evident that TT196 has both stronger outward and inward mass fluxes in the Nightonly and Fullrad experiments while TT202 has weaker fluxes of air inward and outward over a majority of the simulations. However in the Norad experiment, the anomalies are much weaker in magnitude and near zero for a majority of the simulations. The Norad simulations between hours 120 and 144 have stronger mass flux outward in TT196 compared to TT202, but the enhanced outward mass flux is compensated by a weaker inward mass flux in TT196 compared to TT202.

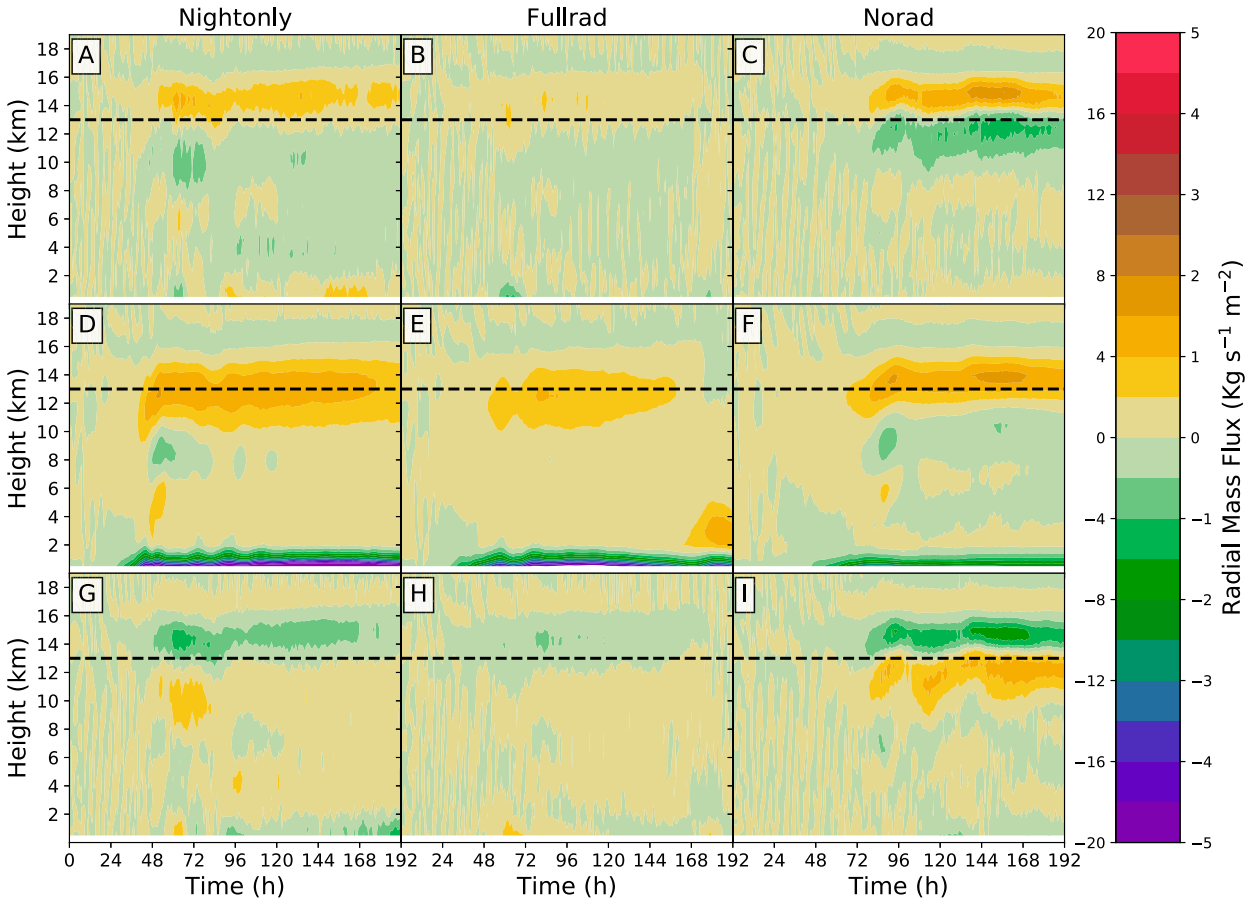

FIG. 8. Axisymmetric mean from the radii 40–100-km mass-weighted radial wind (kg s^{-1} m^{-2}) Hovmöller diagrams for (d) Nightonly, (e) Fullrad, and (f) Norad simulations. (a)–(c) The anomalies of TT196 from the ensemble mean and (g)–(i) the anomalies of TT202. The ensemble means (anomalies) employ values on the left (right) side of the color bar. The dashed black line at 13-km altitude allows for a better comparison of the anomalies and the means.

These results suggest that radiative effects modify the magnitude of the mass transport of the secondary circulation and this modification is primarily responsible for stronger storms with colder upper-tropospheric temperatures.

Figure 10 shows the net radiative tendencies for the Fullrad simulations and the radial wind. There is a maximum in radiative cooling just above the outflow layer that is persistent during both the intensification and peak intensity periods. The upper-level radial outflow and boundary layer inflow both intensify as the storm reaches peak intensity, and the mean longwave cooling increases in area and magnitude. Radiative anomalies in TT196 and TT202 show a dipole with a cooling anomaly over a warming anomaly in TT196 that is reversed in TT202. Radial flow anomalies occur at the location of the vertical gradient in radiative tendencies and intensify along with the radiative anomaly. The dipole is in part due to the cloud tops of the TCs being at different levels but there is also an overall enhancement in the outflow magnitude shown in the radial mass fluxes in Fig. 9. The inflow and outflow dipole produced by an upper-level heat source is consistent with the results of Navarro et al. (2017) using a time-varying equation for the circumferential component of vorticity (Willoughby 2009) similar to the Eliassen equation. There is an enhancement in the radiative tendency means with time but the radiative anomalies and the outflow anomalies remain consistent. Through to the end of the Fullrad simulations, the TT196 and TT202 anomalies in the outflow remain close to 2 m s^{-1}.

The magnitude of radiative cooling in the Nightonly experiments shown in Fig. 11 is noticeably larger than in Fig. 10 since shortwave heating is not offsetting longwave cooling. The ensemble means have stronger inflow and outflow over a larger area compared to the Fullrad simulations. In the radiative anomalies there is a similar dipole as in the Fullrad simulations but the magnitude and areal coverage is larger. There is a stronger response in the outflow, with TT196 having ~10 m s^{-1} stronger outflow than TT202. During the intensification phase,

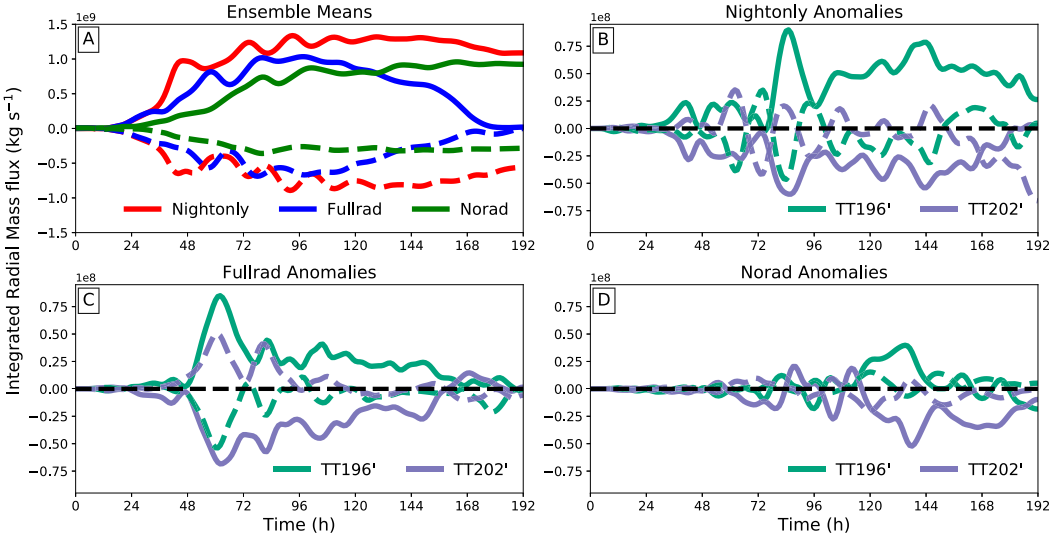

FIG. 9. (a) Integrated radial mass flux from the radii between 0 and 100 km for the ensemble axisymmetric means. Only the (b) Nightonly, (c) Fullrad, and (d) Norad anomalies for TT196 and TT202 are shown for clarity since TT199 is nearly the mean. The solid lines are integrals over the 8–16-km altitudes and dashed lines are the integrals over the 0–3-km altitudes. The black dashed line is the zero anomaly line. Smoothed using 10 iterations of a 1–2–1 filter with weights of 0.25, 0.5, and 0.25, respectively.

the radial wind anomalies are evident in the upper troposphere, but have not yet manifested themselves at low levels. At peak intensity the outflow has weakened slightly and the boundary layer inflow has increased. The outflow anomaly magnitudes have also been slightly reduced, but remain much stronger than the Fullrad anomalies, and the inflow anomalies are apparent at low levels, with TT196 showing enhanced inflow compared to TT202.

The relationship between the radiative and secondary circulation anomalies seen in the Fullrad and Nightonly simulations is consistent with a balanced response to heating and cooling described by the Eliassen equation. Colder upper-tropospheric temperatures result in radiative dipole anomalies with an overall stronger cooling maximum in the longwave tendencies and a stronger secondary circulation, with increased outflow above and inflow below. The anomalies are stronger in the Nightonly simulations, suggesting that the radiative flux divergence causing cloud-top longwave cooling is the primary physical mechanism promoting stronger maximum tangential wind speeds in TT196 versus TT202. The effect is reduced in the Fullrad simulations where cooling is offset by periodic shortwave heating (Schmetz and Beniston 1986), and is not present in the Norad simulations. The results are consistent with Navarro et al. (2017), where upper-level shortwave heating produced local overturning circulations. Upper-level heating anomalies in Navarro et al. (2017), however, did not contribute to stronger tangential winds at the surface, which may be due to the periodicity of the forcing and its concentrated location outside of the RMW. Heating anomalies in the current study extend a large horizontal distance in the upper troposphere, nearly 300 km long at later times in the extensive anvil of the Nightonly simulations (not shown). The expansive area of heating anomalies could contribute to a larger enhancement more similar to that reported by Navarro and Hakim (2016).

Cloud-free radiative cooling could also be a potential mechanism for explaining the intensity differences between the Fullrad and Nightonly simulations (Gray and Jacobson 1977). In the Nightonly simulations the enhanced cloud-free environmental subsidence driven by longwave cooling in the outer environment could force stronger inflow into the TC; however, no substantial differences were present in the outer-core radiative cooling rates over 24-h means (not shown). Due to the short time scale of this study and the large anvil that develops, we hypothesize that this mechanism may play a part in the initial intensity differences between the simulations, but is unlikely to play a major role in the differences between TTL experiments' peak intensities.

5. Applicability of the Carnot conceptual model

In the conceptual model of a TC as a Carnot heat engine, the larger the temperature difference is between the heat source and sink, the greater the thermodynamic efficiency. The outflow temperature is important because it is the mean temperature at which heat is exported from

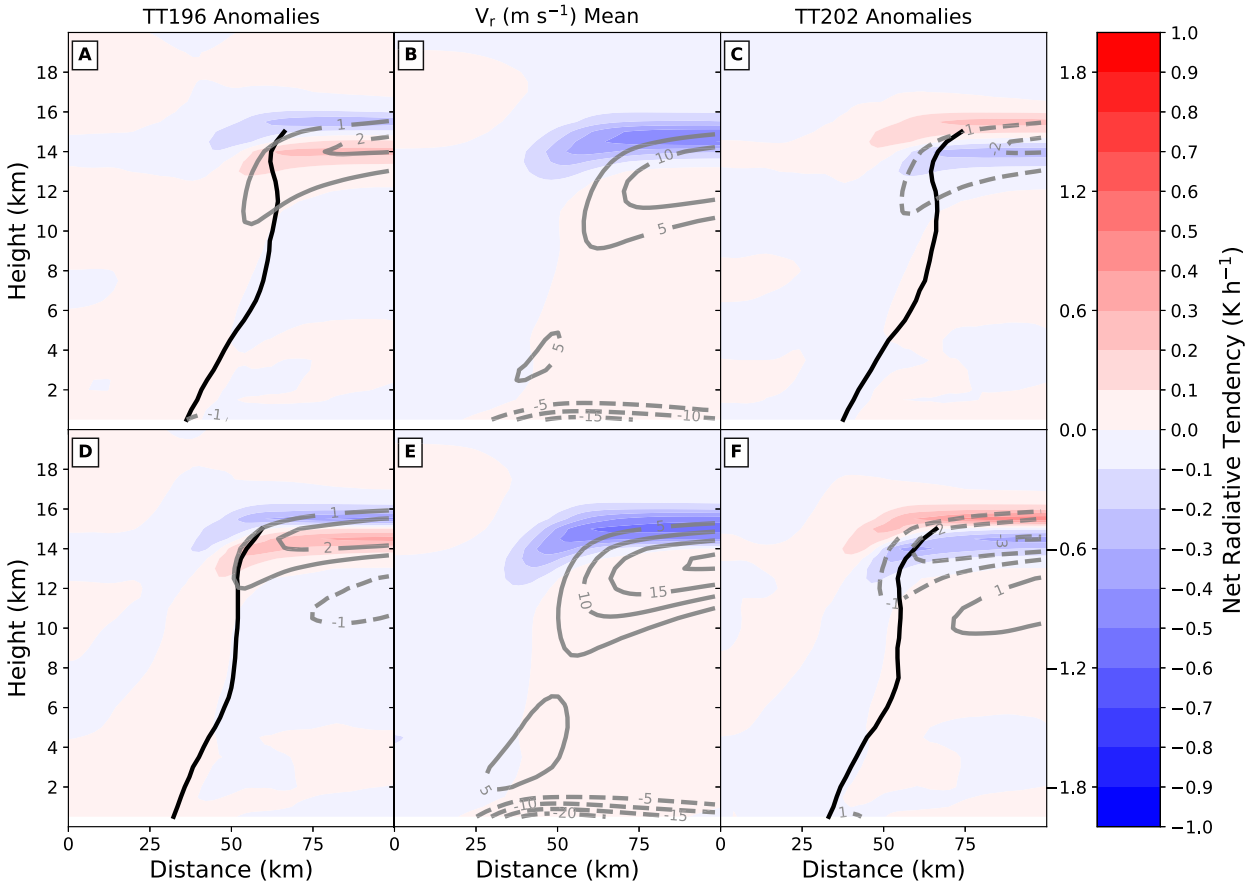

FIG. 10. Axisymmetric mean radial wind (contours) and net radiative tendencies (shaded) for Fullrad simulations for hours (a)–(c) 48–72 and (d)–(f) 72–96. Shown are (b),(e) the ensemble means with radial wind contour intervals of 5 m s^{-1}, (a),(d) the anomalies of TT196 from the ensemble mean, and (c),(f) the anomalies of TT202. The radial wind contour interval is 1 m s^{-1} with the zero line removed from each panel for clarity. Negative radial winds are dashed. Black line indicates RMW up to 15 km.

the TC, which determines the amount of entropy loss in the Carnot cycle (Emanuel 1991). In our experiments, by changing the radiation and the upper-tropospheric temperatures, we have modified both the heat sink and the thermodynamic efficiency. We have also modified the amount of CAPE; however, CAPE is not directly part of the Carnot conceptual model due to the assumption that the vortex is convectively neutral. Differences in CAPE may explain differences in vertical mass flux at upper levels, but CAPE does not explain the differences in maximum intensity of the idealized TCs in the Norad experiment. There exists a ~1% difference in the thermodynamic efficiency as described by the Carnot efficiency between the three TTL experiments with the exact value sensitive to the outflow temperature definition (e.g., Emanuel 1986, 2012). Changes in thermodynamic efficiency cannot explain the intensity differences in the Norad experiments, but the differences in PI are roughly on the same order as the intensity changes in the Nightonly and Fullrad experiments. We examine further here the applicability of the Carnot heat engine model to understand these changes.

In the TC Carnot model, an inflowing parcel of air gains moist entropy in the form of sensible and latent heat from the warm ocean surface in an approximately isothermal expansion as it spirals toward the eyewall. At the RMW the air parcel erupts from the boundary layer and is brought upward and radially outward along a constant angular momentum surface under moist adiabatic expansion to large radii. The parcel then radiatively cools and sinks, such that the cooling is approximately balanced by subsidence warming and the parcel is compressed isothermally. Conceptually, the parcel then converts some latent heat back to sensible heat through evaporation, which further warms and sinks the parcel at constant moist entropy and completes the cycle through adiabatic compression. The cooling and evaporation may take place simultaneously over long time scales of several weeks (Hakim 2011).

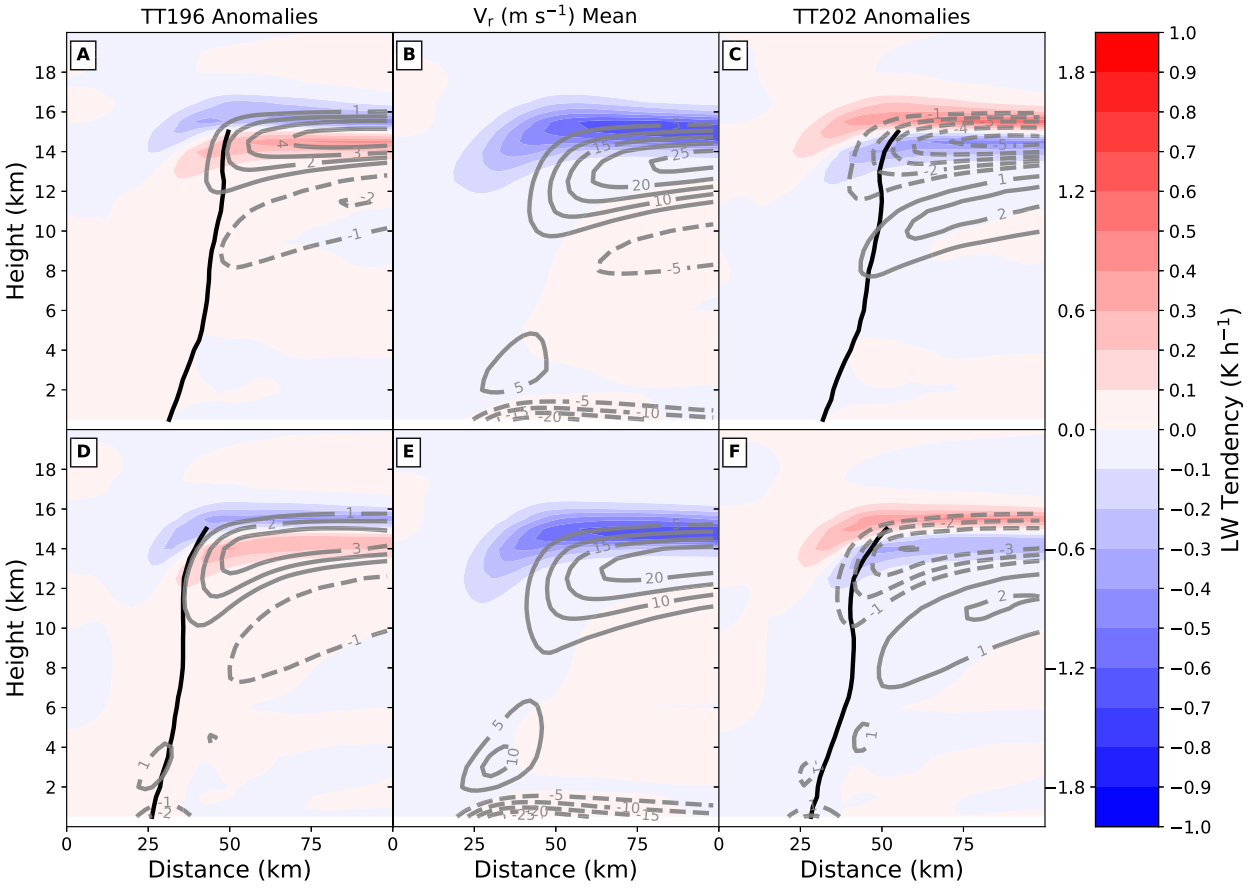

FIG. 11. As in Fig. 10, but for Nightonly simulations.

Both the moist adiabatic expansion and isothermal compression legs of the Carnot cycle are influenced by temperatures and moisture in the middle and upper troposphere (Riemer and Laliberté 2015; Tang and Emanuel 2010; Pauluis 2007). The theoretical Carnot model implicitly assumes that radiation is essentially negligible everywhere except during the isothermal compression leg. By changing the TC depth through decreasing upper-tropospheric temperatures, we are implicitly modifying the adiabatic expansion leg, but we will primarily discuss the isothermal leg where radiative effects are conceptually more important. Although the CPT could be used to approximate the outflow temperature as in past studies (Emanuel et al. 2013), we will not quantify the outflow temperature in each simulation but instead note that the TT196 experiments indeed have the coldest outflow temperature while TT202 has the warmest. Although quantifying the outflow temperature is not necessary for interpreting the results of this study, the effect of different outflow temperature definitions on PI theory will be explored in future work. Outgoing longwave radiation (OLR) acts as the heat sink while subsidence warming counteracts the radiative cooling tendencies. Emanuel (1989) found that when radiative cooling was omitted from their experiment, the maximum winds attained only 85% of their control experiment and that longwave cooling was necessary for a quasi-steady state to be reached. In this sense, shortwave heating is not explicitly included in the conceptual model but could be argued to be implicit in the net radiative cooling.

Figure 12 shows the evolution of the net radiation over the innermost domain for the Nightonly and Fullrad experiments. Over all time periods TT196 has colder upper-tropospheric temperatures so the amount of OLR is reduced, while TT202, which has warmer upper-tropospheric temperatures, has more OLR. These differences also occur in the Fullrad simulations, confirming that the OLR differences are primarily due to differences in upper-tropospheric temperatures. In both sets of experiments the weaker TT202 emits more radiation overall and, therefore, has a stronger radiative heat sink at the top of the atmosphere than the more intense TT196 simulations. In the Fullrad simulations

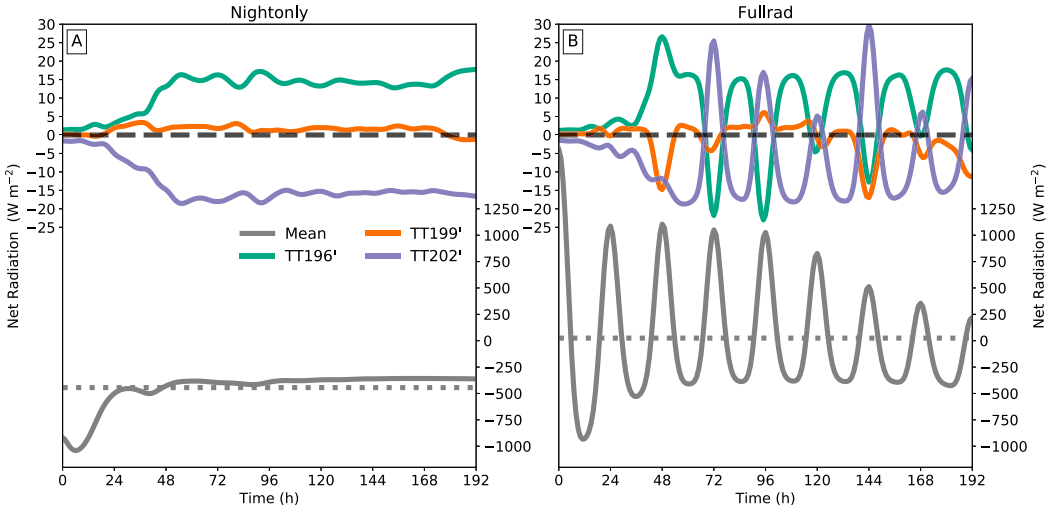

FIG. 12. Integrated net radiation over the innermost domain normalized by the domain size for the (a) Nightonly and (b) Fullrad ensembles. Anomalies are plotted according to the left ordinate for each experiment and the ensemble mean (solid gray) is plotted according to the right ordinate. Negative (positive) mean values indicate a net loss (gain) of energy due to radiation by the system. Gray dotted lines are the time-averaged ensemble-mean values and the black dashed line is where the anomalies are zero. Smoothed using 10 iterations of a 1–2–1 filter with weights of 0.25, 0.5, and 0.25, respectively.

there is less OLR at night in TT196 versus TT202 and less shortwave radiation into the system during the day, indicating that colder upper-tropospheric temperatures cause a reduced response in the diurnal cycle of radiation. The average net radiation is close to zero for the Fullrad experiments, indicating that the effects of both radiation schemes very nearly offset each other in an integrated sense. The reduction in OLR for colder upper-tropospheric temperatures means that less energy can be extracted from the total system, which is opposite of what the higher intensities attained by the TC heat engine would suggest. Given that the heat input is essentially the same in each simulation, this means that in a closed cycle the adiabatic compression leg cannot be completely adiabatic since some additional entropy must then be lost during that leg to close the cycle (Hakim 2011). The change in work from colder TTL temperatures will thus be counteracted by some extent by decreases in OLR.

The thermodynamic efficiency is important for understanding the entropy of the system, but the discrepancy between reduced OLR and higher intensity can be better explained by examining the minimum longwave tendencies (i.e., maximum cooling) for the Nightonly experiments in Fig. 13. The time–radius plot shows that local longwave cooling maximums near cloud top are closely associated with the intensities of each experiment. While the total energy lost to space is reduced with a colder tropopause, the local temperature tendency (K h^{-1}) is enhanced due to the increased radiative flux divergence associated with enhanced ice concentrations at higher altitude. The enhanced ice aloft is due to higher mass flux aloft associated with the colder TTL, but the change in ice and height of the storm does not have a clear relationship with intensity in the Norad simulations. These results suggest that radiation and cloud–radiative feedbacks are critical to understanding the physical mechanism by which colder TTLs affect intensity.

Another possible mechanism by which the upper-tropospheric temperatures might affect the intensity could be from indirectly modifying the heat source through wind-induced sensible and latent heat fluxes from the ocean. Initially stronger storms could yield stronger surface fluxes and potentially produce a positive feedback, but no significant differences were found in integrated surface enthalpy fluxes between the different TTL experiments (not shown). The lack of differences confirms that changes to surface fluxes do not explain the modeled differences in maximum wind speeds found in this study. We also note that the integrated surface enthalpy flux underneath the eyewall is on the order of 10^{14} W, and is an order of magnitude larger than the outgoing radiative flux integrated over the same area that is on the order of 10^{13} W. In a long integration over a large domain in RCE, the clear-sky OLR is large and the integrated fluxes approximately balance, but on the shorter time scales examined here the Carnot cycle cannot be considered "closed" and the conceptual model is incomplete (Riemer and Laliberté 2015).

We argue instead that the Eliassen conceptual model provides a better framework with which to understand the

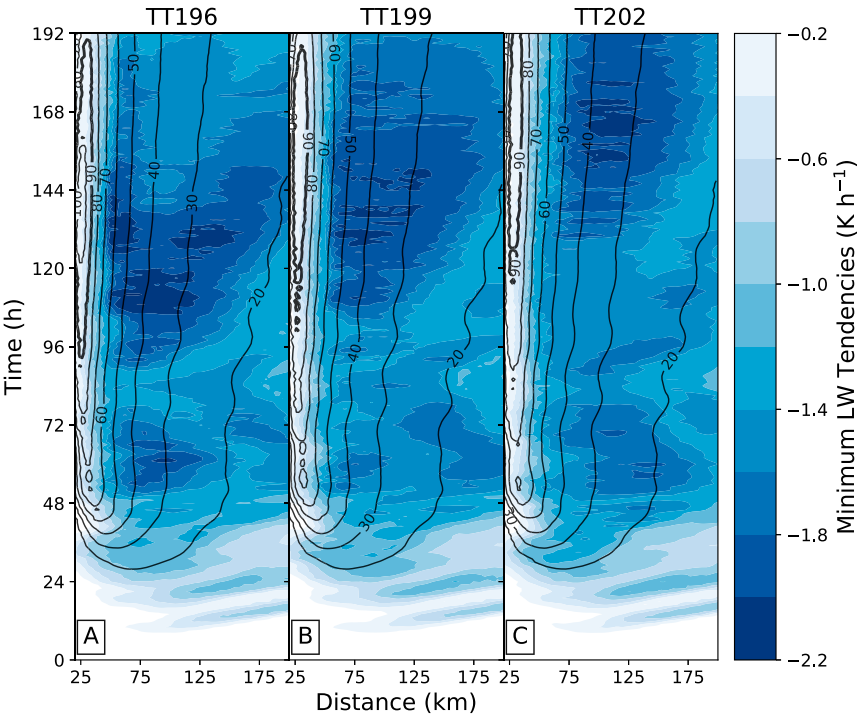

FIG. 13. Hovmöller diagrams of minimum longwave tendencies (shaded; K h^{-1}) and 500-m tangential winds (contours) from the Nightonly axisymmetric ensemble mean for (a) TT196, (b) TT199, and (c) TT202. The tangential winds are contoured every 10 m s^{-1} with values below 20 m s^{-1} removed and 90 m s^{-1} indicated by a thick line.

relationship between radiation and upper-tropospheric temperatures. The radiative heating and cooling dipole anomalies associated with changes in the TTL are well correlated with the changes in integrated radial mass flux, consistent with a balanced response in the secondary circulation associated with diabatic heating in a rapidly rotating vortex. Physically, longwave cooling destabilizes the upper cloud layer on short time scales by enhancing turbulent motion before enhancing cloud-scale motions on longer time scales (Xu and Randall 1995). The vortex responds with a modified secondary circulation that acts to restore thermal wind balance on the system scale. Whether this mechanism is related to the hypothesized turbulent stratification of the outflow (Emanuel 2012) is unclear, but such a mechanism does not need to be invoked to understand the intensity impacts described herein. Further diagnosis of the details of cloud–radiative feedbacks and turbulent processes are beyond the scope of this study, and remain an important area for further research (Tang and Zhang 2016).

6. Discussion and conclusions

In this study, high-resolution simulations of idealized tropical cyclones were conducted to gain a better understanding of how upper-tropospheric temperatures and radiation affect TC intensity and structure. A series of ensemble experiments without radiation, with longwave infrared radiation only, and with full diurnal radiation using different initial conditions from three different tropopause temperatures were performed to investigate the relevant physical mechanisms on weather time scales covering days to about a week. Perturbed moisture fields were used to assess the sensitivity of the results to stochastic changes in convection. The results of these experiments indicate that upper-tropospheric temperatures controlled the amount of upper-level vertical mass flux, ice species aloft, and the height of the TCs on average. Without radiation these changes did not produce a significant modification to the intensity, suggesting that radiation and cloud–radiative feedbacks associated with longwave cooling played a critical role in determining the peak intensity of the TCs.

The results of this study are consistent with the longer-time-scale radiative–convective equilibrium experiments of Wang et al. (2014) and Ramsay (2013) that colder upper-tropospheric temperatures yield stronger TCs when radiative cooling was included; however, the physical mechanism by which the radiation interacted with the TC is distinct. In the RCE experiments in those

studies, Newtonian cooling acts to slowly relax the system back to a prescribed temperature profile over time and does not explicitly include cloud–radiative feedbacks. In the current study, enhanced ice aloft was important in increasing the radiative flux divergence and enhance local cooling rates at cloud top, while actually reducing the total outgoing longwave radiation from the system. From a heat engine perspective, reduced outgoing longwave radiation implies that a colder tropical tropopause layer produces a reduced radiative heat sink in the isothermal compression leg of the Carnot cycle, which would theoretically reduce the work available to the vortex. The reduced radiative heat sink offsets changes to the thermodynamic efficiency, and if the cycle is closed, then entropy must be lost at warmer temperatures during the adiabatic compression leg. A colder tropopause produces a more intense vortex such that the relative change in simulated intensity is still roughly consistent with the predictions of potential intensity theory, albeit with some significant variance in intensity due to ensemble moisture perturbations.

An alternate conceptual model to explain the experiments is through a balanced response in the secondary circulation from the upper-tropospheric radiative cooling and heating anomalies described by the Eliassen equation (Eliassen 1952). Within this framework, the radiative anomaly dipole produced by the higher storm top and enhanced ice aloft induces an enhanced radial outflow as a response to adiabatically return the vortex to thermal wind balance. Increased upper-level vertical and radial mass flux can then increase the low-level inflow through mass continuity and enhance the convergence of absolute angular momentum near the surface. The impact of the cooling anomalies is strongest in the night-only simulations, but is still evident in the full diurnal simulations with a lower magnitude. Without radiation and cloud–radiative feedbacks the change in outflow height does not yield any substantial change in the integrated mass flux at upper or lower levels. Although we have not shown the diagnostic solution to the Eliassen equation from the radiative anomalies herein, the response to the spatial coverage and intensity of the anomalies will be the subject of further work. The magnitude and sign of the responses to upper-level heating and cooling are generally consistent with recent studies by Navarro and Hakim (2016) and Navarro et al. (2017), both in a full-physics axisymmetric model and within a diagnostic Eliassen framework with periodic diurnal forcing. The current study is inherently limited by the idealizations in WRF, but the conceptual model and physical mechanisms described here are applicable to the real atmosphere. Additional complexity in the real atmosphere including asymmetric dynamics, environmental variability in the tropical tropopause layer, and variability in radiative forcing should be considered in future studies.

Finally, we may ask why the simulated intensity scales at roughly the same rate that potential intensity theory predicts given the deficiencies in the Carnot conceptual model interpretation discussed above. We posit that the fundamental assumptions of axisymmetry, thermal wind balance, and slowly evolving flow are the same in potential intensity theory and the Eliassen framework, such that the mathematical definition of the outflow temperature as the upper and outer boundary condition on a rising parcel of air in the eyewall is still a relatively accurate metric to describe the scaling of intensity with tropopause temperature under those assumptions. While the Carnot heat engine provides a useful conceptual framework for describing the energy balance of the boundary layer in such a scenario, the ''thermodynamic efficiency'' is similar to the classical thermodynamic cycle in mathematical form only. The results of this study suggest that this model does not accurately describe the physical mechanism by which the upper troposphere affects the structure and intensity on realistic time scales in the atmosphere; however, the model can still be useful for understanding negative thermodynamic impacts on the heat engine (e.g., Tang and Emanuel 2010; Riemer and Laliberté 2015). Given the idealizations used in this study, further research is warranted to better understand the thermodynamic cycle and role of upper-tropospheric temperatures in real tropical cyclones.

Acknowledgments. This work has been funded by Office of Naval Research Awards N000141613033 and N000141410118. This work has been supported by the Tropical Cyclone Intensity Departmental Research Initiative. The work has benefited from helpful discussions with Michael Riemer. The authors would also like to thank the three anonymous reviewers for their comments and suggestions.

REFERENCES

Bell, M. M., and M. T. Montgomery, 2008: Observed structure, evolution, and potential intensity of category five Hurricane Isabel (2003) from 12 to 14 September. *Mon. Wea. Rev.*, **136**, 2023–2046, https://doi.org/10.1175/2007MWR1858.1.

——, ——, and K. A. Emanuel, 2012: Air–sea enthalpy and momentum exchange at major hurricane wind speeds observed during CBLAST. *J. Atmos. Sci.*, **69**, 3197–3222, https://doi.org/10.1175/JAS-D-11-0276.1.

Bister, M., and K. A. Emanuel, 2002: Low frequency variability of tropical cyclone potential intensity 1. Interannual to interdecadal variability. *J. Geophys. Res.*, **107**, 4801, https://doi.org/10.1029/2001JD000776.

Bu, Y. P., R. G. Fovell, and K. L. Corbosiero, 2014: Influence of cloud–radiative forcing on tropical cyclone structure. *J. Atmos. Sci.*, **71**, 1644–1662, https://doi.org/10.1175/JAS-D-13-0265.1.

Camp, J. P., and M. T. Montgomery, 2001: Hurricane maximum intensity: Past and present. *Mon. Wea. Rev.*, **129**, 1704–1717, https://doi.org/10.1175/1520-0493(2001)129<1704:HMIPAP>2.0.CO;2.

Craig, G., 1996: Numerical experiments on radiation and tropical cyclones. *Quart. J. Roy. Meteor. Soc.*, **122**, 415–422, https://doi.org/10.1002/qj.49712253006.

Dudhia, J., 1989: Numerical study of convection observed during the Winter Monsoon Experiment using a mesoscale two-dimensional model. *J. Atmos. Sci.*, **46**, 3077–3107, https://doi.org/10.1175/1520-0469(1989)046<3077:NSOCOD>2.0.CO;2.

Dunion, J. P., C. D. Thorncroft, and C. S. Velden, 2014: The tropical cyclone diurnal cycle of mature hurricanes. *Mon. Wea. Rev.*, **142**, 3900–3919, https://doi.org/10.1175/MWR-D-13-00191.1.

Eliassen, A., 1952: Slow thermally or frictionally controlled meridional circulations in a circular vortex. *Astrophys. Nor.*, **5**, 19–60.

Emanuel, K. A., 1986: An air–sea interaction theory for tropical cyclones. Part I: Steady-state maintenance. *J. Atmos. Sci.*, **43**, 585–604, https://doi.org/10.1175/1520-0469(1986)043<0585:AASITF>2.0.CO;2.

——, 1988: The maximum intensity of hurricanes. *J. Atmos. Sci.*, **45**, 1143–1155, https://doi.org/10.1175/1520-0469(1988)045<1143:TMIOH>2.0.CO;2.

——, 1989: The finite-amplitude nature of tropical cyclogenesis. *J. Atmos. Sci.*, **46**, 3431–3456, https://doi.org/10.1175/1520-0469(1989)046<3431:TFANOT>2.0.CO;2.

——, 1991: The theory of hurricanes. *Annu. Rev. Fluid Mech.*, **23**, 179–196, https://doi.org/10.1146/annurev.fl.23.010191.001143.

——, 2012: Self-stratification of tropical cyclone outflow. Part II: Implications for storm intensifications. *J. Atmos. Sci.*, **69**, 988–996, https://doi.org/10.1175/JAS-D-11-0177.1.

——, S. Solomon, D. Folini, S. Davis, and C. Cagnazzo, 2013: Influence of tropical tropopause layer cooling on Atlantic hurricane activity. *J. Climate*, **26**, 2288–2301, https://doi.org/10.1175/JCLI-D-12-00242.1.

Fovell, R. G., K. L. Corbosiero, and H.-C. Kuo, 2009: Cloud microphysics impact on hurricane track revealed in idealized experiments. *J. Atmos. Sci.*, **66**, 1764–1778, https://doi.org/10.1175/2008JAS2874.1.

——, K. L. Bu, Y. P. Corbosiero, W. Tung, Y. Cao, H. Kuo, L. Hsu, and H. Su, 2016: Influence of cloud microphysics and radiation on tropical cyclone structure and motion. *Multiscale Convection-Coupled Systems in the Tropics: A Tribute to Dr. Michio Yanai*, *Meteor. Monogr.*, No. 56, Amer. Meteor. Soc., https://doi.org/10.1175/AMSMONOGRAPHS-D-15-0006.1.

Gettelman, A., and P. F. Forster, 2002: A climatology of the tropical tropopause layer. *J. Meteor. Soc. Japan*, **80**, 911–924, https://doi.org/10.2151/jmsj.80.911.

Godbole, R. V., 1973: On destabilization of clouds by radiative cooling. *Mon. Wea. Rev.*, **101**, 496–500, https://doi.org/10.1175/1520-0493(1973)101<0496:ODOCBR>2.3.CO;2.

Gray, W. M., and R. W. Jacobson Jr., 1977: Diurnal variation of deep cumulus convection. *Mon. Wea. Rev.*, **105**, 1171–1188, https://doi.org/10.1175/1520-0493(1977)105<1171:DVODCC>2.0.CO;2.

Hakim, G. J., 2011: The mean state of axisymmetric hurricanes in statistical equilibrium. *J. Atmos. Sci.*, **68**, 1364–1376, https://doi.org/10.1175/2010JAS3644.1.

Hirschberg, P. A., and J. M. Fritsch, 1993: On understanding height tendency. *Mon. Wea. Rev.*, **121**, 2646–2661, https://doi.org/10.1175/1520-0493(1993)121<2646:OUHT>2.0.CO;2.

Holland, G. J., 1997: The maximum potential intensity of tropical cyclones. *J. Atmos. Sci.*, **54**, 2519–2541, https://doi.org/10.1175/1520-0469(1997)054<2519:TMPIOT>2.0.CO;2.

Hong, S.-Y., Y. Noh, and J. Dudhia, 2006: A new vertical diffusion package with an explicit treatment of entrainment processes. *Mon. Wea. Rev.*, **134**, 2318–2341, https://doi.org/10.1175/MWR3199.1.

Melhauser, C., and F. Zhang, 2014: Diurnal radiation cycle impact on the pregenesis environment of Hurricane Karl (2010). *J. Atmos. Sci.*, **71**, 1241–1259, https://doi.org/10.1175/JAS-D-13-0116.1.

Mlawer, E. J., S. J. Taubman, P. D. Brown, M. J. Iacono, and S. A. Clough, 1997: Radiative transfer for inhomogeneous atmospheres: RRTM, a validated correlated-k model for the longwave. *J. Geophys. Res.*, **102**, 16 663–16 682, https://doi.org/10.1029/97JD00237.

Navarro, E. L., and G. J. Hakim, 2016: Idealized numerical modeling of the diurnal cycle of tropical cyclones. *J. Atmos. Sci.*, **73**, 4189–4201, https://doi.org/10.1175/JAS-D-15-0349.1.

——, ——, and H. E. Willoughby, 2017: Balanced response of an axisymmetric tropical cyclone to periodic diurnal heating. *J. Atmos. Sci.*, **74**, 3325–3337, https://doi.org/10.1175/JAS-D-16-0279.1.

Nicholls, M. E., 2015: An investigation of how radiation may cause accelerated rates of tropical cyclogenesis and diurnal cycles of convective activity. *Atmos. Chem. Phys.*, **15**, 9003–9029, https://doi.org/10.5194/acp-15-9003-2015.

Nolan, D. S., 2007: What is the trigger for tropical cyclogenesis? *Aust. Meteor. Mag.*, **56**, 241–266.

Ohno, T., M. Satoh, and Y. Yamada, 2016: Warm cores, eyewall slopes, and intensities of tropical cyclones simulated by a 7-km-mesh global nonhydrostatic model. *J. Atmos. Sci.*, **73**, 4289–4309, https://doi.org/10.1175/JAS-D-15-0318.1.

Pauluis, O., 2007: Sources and sinks of available potential energy in a moist atmosphere. *J. Atmos. Sci.*, **64**, 2627–2641, https://doi.org/10.1175/JAS3937.1.

Ramsay, H. A., 2013: The effects of imposed stratospheric cooling on the maximum intensity of tropical cyclones in axisymmetric radiative–convective equilibrium. *J. Climate*, **26**, 9977–9985, https://doi.org/10.1175/JCLI-D-13-00195.1.

Riemer, M., and F. Laliberté, 2015: Secondary circulation of tropical cyclones in vertical wind shear: Lagrangian diagnostic and pathways of environmental interaction. *J. Atmos. Sci.*, **72**, 3517–3536, https://doi.org/10.1175/JAS-D-14-0350.1.

Rotunno, R., and K. A. Emanuel, 1987: An air–sea interaction theory for tropical cyclones. Part II: Evolutionary study using a nonhydrostatic axisymmetric numerical model. *J. Atmos. Sci.*, **44**, 542–561, https://doi.org/10.1175/1520-0469(1987)044<0542:AAITFT>2.0.CO;2.

Saha, S., and Coauthors, 2010: The NCEP Climate Forecast System Reanalysis. *Bull. Amer. Meteor. Soc.*, **91**, 1015–1057, https://doi.org/10.1175/2010BAMS3001.1.

Schmetz, J., and M. Beniston, 1986: Relative effects of solar and infrared radiative forcing in a mesoscale model. *Bound.-Layer Meteor.*, **34**, 137–155, https://doi.org/10.1007/BF00120913.

Seidel, D. J., R. Ross, J. K. Angell, and G. C. Reid, 2001: Climatological characteristics of the tropical tropopause as revealed by radiosondes. *J. Geophys. Res.*, **106**, 7857–7878, https://doi.org/10.1029/2000JD900837.

Skamarock, W. C., and Coauthors, 2008: A description of the Advanced Research WRF version 3. NCAR Tech. Note NCAR/TN-475+STR, 113 pp., https://dx.doi.org/10.5065/D68S4MVH.

Sui, C.-H., A. Li, and K.-M. Lau, 1998: Radiative–convective processes in simulated diurnal variations of tropical oceanic convection. *J. Atmos. Sci.*, **55**, 2345–2357, https://doi.org/10.1175/1520-0469(1998)055<2345:RCPISD>2.0.CO;2.

Tang, B., and K. A. Emanuel, 2010: Midlevel ventilation's constraint on tropical cyclone intensity. *J. Atmos. Sci.*, **67**, 1817–1830, https://doi.org/10.1175/2010JAS3318.1.

Tang, X., and F. Zhang, 2016: Impacts of the diurnal radiation cycle on the formation, intensity, and structure of Hurricane Edouard (2014). *J. Atmos. Sci.*, **73**, 2871–2892, https://doi.org/10.1175/JAS-D-15-0283.1.

——, Z. Tan, J. Fang, Q. Sun, and F. Zhang, 2017: Impacts of diurnal radiation cycle on secondary eyewall formation. *J. Atmos. Sci.*, **74**, 3079–3098, https://doi.org/10.1175/JAS-D-17-0020.1.

Thompson, G., and T. Eidhammer, 2014: A study of aerosol impacts on clouds and precipitation development in a large winter cyclone. *J. Atmos. Sci.*, **71**, 3636–3658, https://doi.org/10.1175/JAS-D-13-0305.1.

Tiedtke, M., 1989: A comprehensive mass flux scheme for cumulus parameterization in large-scale models. *Mon. Wea. Rev.*, **117**, 1779–1800, https://doi.org/10.1175/1520-0493(1989)117<1779:ACMFSF>2.0.CO;2.

Van Sang, N., R. K. Smith, and M. T. Montgomery, 2008: Tropical cyclone intensification and predictability in three dimensions. *Quart. J. Roy. Meteor. Soc.*, **134**, 563–582, https://doi.org/10.1002/qj.235.

Wang, S., S. J. Camargo, A. H. Sobel, and L. M. Polvani, 2014: Impact of the tropopause temperature on the intensity of tropical cyclones: An idealized study using a mesoscale model. *J. Atmos. Sci.*, **71**, 4333–4348, https://doi.org/10.1175/JAS-D-14-0029.1.

Willoughby, H. E., 2009: Diabatically induced secondary flows in tropical cyclones. Part II: Periodic forcing. *Mon. Wea. Rev.*, **137**, 822–835, https://doi.org/10.1175/2008MWR2658.1.

Xu, K.-M., and D. A. Randall, 1995: Impact of interactive radiative transfer on the macroscopic behavior of cumulus ensembles. Part II: Mechanisms for cloud–radiation interactions. *J. Atmos. Sci.*, **52**, 800–817, https://doi.org/10.1175/1520-0469(1995)052<0800:IOIRTO>2.0.CO;2.